

# Lab on a Chip

Accepted Manuscript



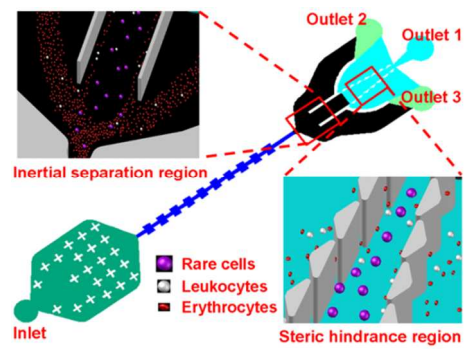
This is an *Accepted Manuscript*, which has been through the Royal Society of Chemistry peer review process and has been accepted for publication.

*Accepted Manuscripts* are published online shortly after acceptance, before technical editing, formatting and proof reading. Using this free service, authors can make their results available to the community, in citable form, before we publish the edited article. We will replace this *Accepted Manuscript* with the edited and formatted *Advance Article* as soon as it is available.

You can find more information about *Accepted Manuscripts* in the [Information for Authors](#).

Please note that technical editing may introduce minor changes to the text and/or graphics, which may alter content. The journal's standard [Terms & Conditions](#) and the [Ethical guidelines](#) still apply. In no event shall the Royal Society of Chemistry be held responsible for any errors or omissions in this *Accepted Manuscript* or any consequences arising from the use of any information it contains.

## Graphical abstract



We present a multistage microfluidic device for continuous label-free separation of rare cells using a combination of inertial microfluidics and steric hindrance.

Cite this: DOI: 10.1039/c0xx00000x

www.rsc.org/xxxxxx

PAPER

## High-throughput rare cell separation from blood samples using steric hindrance and inertial microfluidics†

Shaofei Shen,<sup>a</sup> Chao Ma,<sup>b</sup> Lei Zhao,<sup>b</sup> Yaolei Wang,<sup>a</sup> Jian-Chun Wang,<sup>a</sup> Juan Xu,<sup>a</sup> Tianbao Li,<sup>a</sup> Long Pang<sup>b</sup> and Jinyi Wang<sup>\*ab</sup>

5 Received (in XXX, XXX) Xth XXXXXXXXX 20XX, Accepted Xth XXXXXXXXX 20XX  
DOI: 10.1039/b000000x

Presence and quantity of rare cells in the bloodstream of cancer patients provide a potentially accessible source for early detection of invasive cancer and treatment monitoring of advanced diseases. Separation of rare cells from peripheral blood, as a “virtual and real-time liquid biopsy”, is expected to replace  
10 conventional tissue biopsies of metastatic tumors for therapy guidance. However, technical obstacles similar to looking for a needle in a haystack, have hindered the broad clinical utility of this method. In this study, we developed a multistage microfluidic device for continuous label-free separation and enrichment of rare cells from blood samples based on cell size and deformability. We successfully separated tumor cells (MCF-7 and HeLa cells) and leukemic (K562) cells spiked in diluted whole blood  
15 using a unique complementary combination of inertial microfluidics and steric hindrance in a microfluidic system. The processing parameters of the inertial focusing and steric hindrance regions were optimized to achieve high-throughput and high-efficiency separation, a significant advantage compared with existing rare cell isolation technologies. The results from experiments with rare cells spiked in 1% hematocrit blood indicated > 90% cell recovery at a throughput of  $2.24 \times 10^7$  cells/min. The impressive enrichment  
20 of rare cells was  $> 2.02 \times 10^5$ -fold. Thus, this microfluidic system driven by purely hydrodynamic forces has practical potential to be applied either alone or as a sample preparation platform for fundamental studies and clinical applications.

### Introduction

Compared with surgical biopsies using fresh tissue, blood  
25 examination is less invasive and easier to routinely perform for various health tests due to accessibility and convenience of blood collection.<sup>1</sup> In addition, some low-abundance rare cells, such as leukemic cells and circulating tumor cells (CTCs), are found in the peripheral blood of cancer patients.<sup>2</sup> The presence and  
30 quantity of these rare cells are highly correlated with cancer metastasis and treatment analysis.<sup>2,3</sup> In particular, 90% of all cancer-related deaths are caused by cancer metastasis. However, primary tumor sampling cannot promptly and accurately reflect the actual metastatic conditions or recurrence of cancer at an  
35 early stage,<sup>4,5</sup> indicating an emerging need to precisely separate and detect rare cells that serve as representative surrogate tumor biomarkers for real-time monitoring and personalized therapy. The availability of blood sample assay as a “virtual and real-time liquid biopsy” is beneficial for rare cell enumeration and  
40 characterization with respect to biological properties using current techniques. Thus, this process has been envisioned to replace conventional tissue biopsies of metastatic tumors and to revolutionize cancer diagnosis and treatment monitoring.<sup>6</sup> However, processing and analyzing low-abundance rare cells  
45 from peripheral blood (~1 to 100 rare cells per  $10^9$  blood cells)

present an obvious challenge because of the complex nature of blood and the rarity of target cells, similar to fishing for a needle in a haystack.<sup>2,6</sup> Thus, a highly specialized separation or enrichment step is necessary to harvest high-purity and viable  
50 rare cells suitable for subsequent downstream (molecular) analysis.<sup>7</sup>

Current conventional macroscale approaches for rare cell fishing from blood samples are limited to labor-intensive, inefficient, and high-cost methods, such as physical filtration and  
55 density gradient centrifugation, or combined with red blood cell lysis for extracting mononuclear cells, immunomagnetic-assisted cell sorting, and fluorescence-activated cell sorting. These techniques are further complicated by the requirement of multiple batch complex procedures that result in cell contamination or  
60 substantial loss of cancer cells, lack of high efficiency and specificity due to the extremely low number of rare cells, and identification interference caused by aggressive rare cell subpopulations with reduced expression of epithelial markers; the latter phenomenon is ascribed to the epithelial–mesenchymal  
65 transition, which may underestimate the number of actual rare cells presented in the bloodstream, giving rise to wrong expectations in clinical studies.<sup>8–10</sup> Thus, simpler, less expensive, and more efficient techniques must be developed to separate and enrich sensitive rare cells from blood samples conveniently and

rapidly for subsequent analysis in tumor research and clinical diagnostics.

With the rapid progress of promising microfluidic technologies, much attention on blood analysis has been directed to microfluidic devices due to their small scale, simplicity of fabrication and automation, and excellent performance in controlling the blood microenvironment and processing complex blood cells.<sup>6,11–13</sup> Furthermore, isolated rare cells can be applied for subsequent on-chip cell culture or downstream (molecular) analysis as part of the rare cell separation process, eliminating the intermediate operation steps and accelerating the overall rare cell characterization procedures required in macroscale approaches.<sup>11</sup> Microfluidic-based rare cell separation systems have been increasingly studied with various proposed rare cell isolation mechanisms: cell-affinity micro-chromatography,<sup>14</sup> cellular biophysics-based isolation,<sup>15</sup> magnetic forces,<sup>16</sup> and dielectrophoresis.<sup>17</sup> However, a major limitation of on-chip blood processing for analysis of rare cells is low processing throughput (<10<sup>6</sup> cells/min), either because of low operational flow rates or high whole blood viscosity, making them unsuitable for processing rare cell separation in clinical blood samples.<sup>2</sup>

Researchers have shown that high-speed and precise particle/cell manipulation focuses at distinct positions in microchannels (henceforth known as inertial microfluidics) using inertial forces intrinsic to particle motion in confined channel flows.<sup>18–20</sup> The throughput of hydrodynamic sorting technique based on inertial microfluidics is very high without the application of external forces, and thus, may be suitable for rare cell separation from large numbers of various cell-contained blood samples. Therefore, in our initial efforts, we attempted to construct a simple hydrodynamic method for particle/cell separation by introducing inertial microfluidics in a microfluidic device, in which contracting and expanding channels in turns and series were used to create a multi-orifice flow fractionation (MOFF). Theoretically, this kind of device has greater potential for cell separation in a high-throughput manner than other microfluidic separators, and can be easily combined with either upstream or downstream applications to construct more complex lab-on-a-chip systems for addressing medical and biological issues. However, high-purity separation of rare cells from human complex blood using only inertial microfluidics remains challenging. This difficulty may be due to the fact that malignant tumor cells, different from benign tumor cells, have irregular shapes and can grow rapidly.<sup>21</sup> Moreover, different rare cell types and different rare cell sub-types lead to cell possessing different characteristics, such as variations in size, shape and viscoelastic rheological properties.<sup>22</sup> Studies have demonstrated that the use of steric hindrance separation technique has great potential in cell separation. To date, various steric hindrance-based microfluidic devices have been developed, such as dead-end or crossflow filtration barrier device,<sup>23–25</sup> dynamic microchannel device,<sup>26</sup> multi-obstacle architecture filter device<sup>14</sup> and microfluidic funnel ratchets device.<sup>27</sup> These efforts have greatly enhanced rare cell separation. However, the steric hindrance-based devices are often clogged during direct processing of complex blood samples, which complicates the process for obtaining statistically and quantitatively significant data and for further clinical applications.

Based on the analysis above, we present a multistage microfluidic device by combining inertial microfluidics with steric hindrance in turn. The use of inertial microfluidics can efficiently divide target cells and other cells into different groups and guide their movement in their respective trajectories. When the cells in different movement trajectories enter the steric hindrance region, masses of non-target cells are removed with the help of inertial microfluidics and a primary steric hindrance unit, greatly eliminating the blockage problem in the subsequent steric hindrance separation. To further purify the target cells, an isosceles trapezoid-shaped pillar array railing ( $\mu$ ITPAR) functioning as a second steric hindrance unit was also integrated in the steric hindrance region, functioning as a re-focusing and re-purifying unit. We first investigated the separation mechanism and performance of the designed device using theoretical calculations and fluorescence-labeled microspheres. Simultaneously, the optimal conditions for cell separation were also explored. Afterward, the removal of blood cells and the enrichment of tumor cells (MCF-7 and HeLa cells) and leukemic (K562) cells spiked in diluted whole blood were performed using the optimized microfluidic device.

## Experimental

More detailed information on the materials and methods used can be found in the Supplementary Information.

### Device design

The device comprised four functional regions: (i) filter region, (ii) inertial focusing region, (iii) inertial separation region, and (iv) steric hindrance region. Fig. 1 shows the schematic of the microfluidic device structure and the high-throughput separation processes of rare cells in the microfluidic device. The use of the designed filter region (Fig. 1A), which effectively prevents the subsequent channel clogging caused by cell aggregates or foreign debris, was critical in handling high volume of blood samples.<sup>28</sup> The inertial focusing region (Fig. 1B) was composed of 80 repeated contraction/expansion channel units with total length of 2.4 cm. The contraction and the expansion channels were both 150  $\mu$ m long. Each expansion channel had a width of 180  $\mu$ m, whereas the contraction channel was designed in three different dimensions, 30, 60, and 90  $\mu$ m, to investigate the focusing effect of the inertial focusing region. The height of the channels and microstructures of the device were all 57  $\mu$ m. The main channel in the inertial separation region (Fig. 1C) was split into two side channels and one central channel by the steric hindrance structures. The two side channels were respectively connected with outlets 2 and 3 for exiting small-sized cells (blood cells). The central channel was connected with outlet 1 for collecting large-sized target cells (rare cells). The expansion-shaped design with rapidly increasing angle, an important parameter for controlling separation amplification in the inertial separation region, promoted the shift of the particle/cell equilibrium position to the centerline.<sup>29</sup> The steric hindrance region (Fig. 1D) involving periodically spaced isosceles trapezoid-shaped pillars [for the detailed description of the designed devices (Devices 1, 2, and 3), see Fig. S1 and Table S1 in ESI†] removed the unseparated blood components to improve target cell separation efficiency.

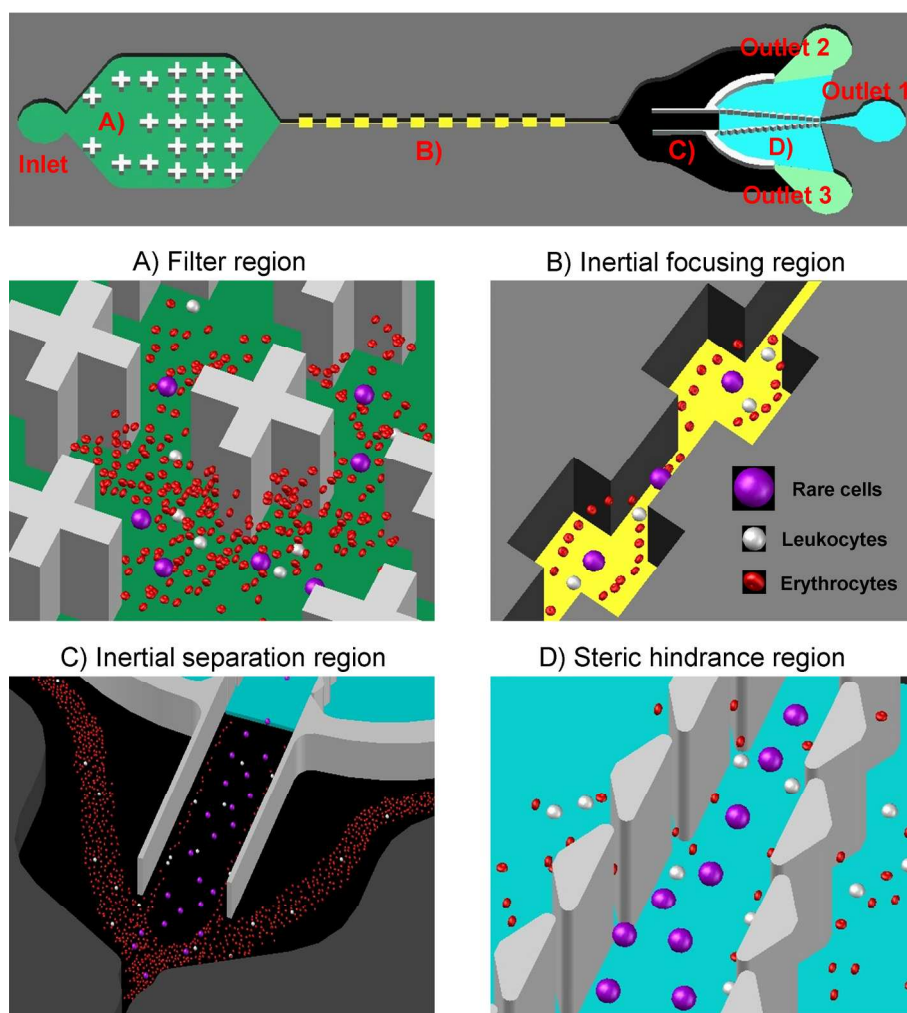


**Fig. 1** Schematic diagram of the designed microfluidic device for rare cell isolation using steric hindrance and inertial microfluidics. The filter region (A) can effectively block foreign debris to avoid downstream clogging in microchannels. Under the influence of inertial lift forces and unique secondary flow in the inertial focusing region (B), relatively larger rare cells and a few blood cells pass through the center channel of the inertial separation region (C) and enter the steric hindrance region (D), whereas most blood cells exit through outlets 2 and 3. Subsequently, based on cell size and deformability in the steric hindrance region, the isosceles trapezoid-shaped pillar array railing ( $\mu$ ITPAR) can further remove the unseparated blood components and enrich rare cells through outlet 1.

### Cell viability assay

Cell viabilities before and after isolation were assessed by using a common acridine orange (AO) and propidium iodide (PI) double-staining protocol.<sup>30</sup> After removing the growth medium and rinsing with PBS, the AO/PI (5  $\mu$ g/mL in PBS) staining solution was introduced into the cell samples, and the staining process was performed for 10 min at room temperature. Afterward, PBS was introduced for 15 min as a final rinse.

### Experimental setup

During each experiment, the microsphere/cell sample was pumped into the microfluidic device at varying channel Reynolds numbers using a syringe pump (Longer pump, LSP01-1A) to generate a stable and continuous microflow. A 10 mL syringe was connected to the inlet (diameter: 2 mm) of the device using Tygon tubing (internal diameter: 0.42 mm; length: 25 cm). Prior

to use, the device system was initially irradiated with UV light for 1 h, and then sequentially rinsed with 70% ethanol, followed by ultra-purified water and PBS working buffer.

### Microscopy and image analysis

An inverted microscope (Olympus, CKX41) with a charge coupled device camera (Olympus, DP72) and a mercury lamp (Olympus, URFLT50) was used to obtain phase contrast and fluorescence images. Time-lapse images of the samples were obtained every 1 s. A total of 100 to 200 images were overlaid to create each averaged composite image. Image and data analyses were performed using Image-Pro<sup>®</sup> Plus 6.0 (Media Cybernetics, Silver Spring, MD) and SPSS 12.0 (SPSS Inc.) software, respectively. The results and error bars in the graphs are expressed as the mean  $\pm$  SD. Tests of data significance were performed using one-way analysis of variance (ANOVA).

## Results and discussion

### Theory and mechanism

In a microfluidic channel, the microspheres/cells suspended in a fluid are subjected to both inertial lift and viscous drag forces.<sup>19</sup>

Normally, we can interpret these occurrences using Reynolds number ( $Re$ ), a dimensionless number that provides a measure of the ratio of the inertial forces to viscous force, characterizing the fluid dynamic phenomenon in the microchannel. In addition, we can describe the motion of the particles flowing through a microchannel using the particle Reynolds number ( $Re_p$ ) as follows:

$$Re_p = Re_c \frac{d^2}{D_h^2} = \frac{\rho U_m d^2}{\mu D_h} \quad (1)$$

where  $Re_c$  is the channel Reynolds number,  $d$  is the particle diameter,  $\rho$  is the density of the fluid,  $\mu$  is the dynamic viscosity of the fluid, and  $U_m$  is the maximum flow velocity in the channel. Moreover, the hydraulic diameter of the channel  $D_h$  is defined as follows:

$$D_h = \frac{2HW}{H+W} \quad (2)$$

where  $H$  and  $W$  are the height and width of the channel, respectively. Notably,  $Re_c$  uses maximum velocity instead of mean velocity that is normally applied for  $Re$ . When  $Re_p \gg 1$ , the inertial lift force becomes a dominant parameter for driving the lateral migration of particles transverse to the fluid streamlines. Meanwhile, when  $Re_p \ll 1$ , the viscous drag force acting on the particle surface has an important role in longitudinal particle migration in the microfluidic channel.<sup>31</sup>

The size-based rigid particle separation in a radially asymmetric microchannel is operated by a combination of three fluid-mechanical lift forces: a shear-gradient-induced lift force, a wall effect-induced lift force, and a rotation-induced lift force.<sup>32,33</sup> The equilibrium position of uniformly dispersed rigid particles is achieved by the balance of the three lift forces. The shear gradient-induced lift force produced by the parabolic laminar velocity profile in plane Poiseuille flow drives rigid particle migration toward the channel walls. However, when the rigid particles migrate closer to the channel wall, a counteracting wall-induced lift pushes these particles away, primarily because the fluid velocity and the asymmetric wake vorticity generated at the surface of the rigid particles induce higher pressure on the wall side than on the centerline side. After the two opposing lift forces balanced each other, the rotation-induced lift force acts directionally on the rigid particles, generating a net force along the wall toward the channel center. The rigid particles then migrate to the stable equilibrium positions centered at the faces where limited spinning arises due to minimum shear rate.<sup>33,34</sup> Deformable particles/cells can induce nonlinear lateral migration due to deformation-induced lift force, aside from the nonlinearity related to the inertia of the fluid. Deformation-induced lift force is generated due to the matching of velocities and stresses at the deformable particle/cell interface. The magnitude of the lateral drift velocity and lift force is closely associated with the deformed shape of the particles/cells. Consequently, aside from

the above three fluid-mechanical lift forces, the deformation-induced lift force will act on the deformed particles/cells to produce modified stable equilibrium positions.<sup>35</sup>

Furthermore, the size-based particle/cell separation in a multi-orifice microchannel is also driven by a secondary flow.<sup>34,36,37</sup> As a consequence of a series of alternating narrow (contracting) and wide (expanding) channel geometry, a unique vortex will arise under low  $Re_c$  at the corners of the expansion channels. Interestingly, the presence of vortices in an orifice channel is slightly different from that in the straight channel generated by high  $Re_c$ ,<sup>38</sup> and vastly different from that of the Dean vortex created in a curved channel at low  $Re_c$ ,<sup>39</sup> or the vortex created in asymmetrically structured microchannels.<sup>40,41</sup> Vortex formation relies on several factors, including the ratio between contracting and expanding channel cross-section areas, angle and roundness of the orifice corner, surface roughness and fluid inertia.<sup>31</sup> Notably, the fluid inertia depends primarily on  $Re_c$ . However, the increasing  $Re_c$  of the fluid increases the vortex size until the full-expansion region is occupied.<sup>41</sup> To explore the vortex distribution in the microchannel of the current device, a numerical simulation was performed using ESI-CFD software under different experimental conditions.

As shown in Fig. S2A (ESI†), under different  $Re_c$ , obvious vortex variations were observed along with the change of the fluid velocity in the vortex region. When  $Re_c = 27.78$ , a small vortex zone appeared near the entrance of the expansion chamber, occupying about 1/3 of the expansion channel cavity. A significant vortex zone was observed when  $Re_c > 50$  due to the sudden expanding and contracting channel, covering almost half of the cavity area. When the  $Re_c$  was more than 72.22, the vortex flow expanded up to almost all of the cavity area. Quantitative analysis (Fig. S2B, ESI†) of the numerical simulation images showed that the fluid velocity in the vortex region increased with the increase in  $Re_c$ , and the position of the maximum flow velocity in the vortex zone became stable and uniform. With the increase in  $Re_c$ , the rising ratio of the flow velocity to the maximum flow velocity was the same along the direction of the microflow in the same position of the vortex region. However, upon reaching the maximum value of the ratio, the difference in the ratio decreased (Fig. S2C, ESI†). Consequently, we believe that the large size particles/cells form into a nearly linear pattern without severe sudden turns at a certain  $Re_c$  in the expansion chamber due to the presence of the vortex region, seeming to pass through a straight channel. We simulated the fluid velocity distribution of the inertial separation region with a specific range of  $Re_c$  (Figs. S3A and B, ESI†), which showed that the fluid velocity of the central channel region is higher than those of the two side channels at the same  $Re_c$ . Interestingly, we found that a lower ratio of flow velocity to maximum flow velocity can occur in the inertial separation region when  $Re_c$  was in the range of 50 to 72.22 (Figs. S3A and C, ESI†). To the best of our knowledge, this phenomenon has not been previously reported. These results demonstrate that the fluid is inclined to flow toward the central channel region when the  $Re_c$  ranges from 50 to 72.22.

Mass conservation requires that the time rate of the change in mass in a control volume is balanced by the net mass that flows into the same control volume (inflow-outflow). The physical meaning is that the relative expansion rate of the fluid volume is

equal to the relative decrease rate of the fluid density in any point of the incompressible flow field. Formula (2) is the continuity equation in differential form for incompressible flow, and the well-known integral form of continuity equation can be expressed as follows:

$$\sum V_1 A_1 = \sum V_2 A_2 \quad (3)$$

where  $V_1$  and  $V_2$  are the mean velocity of the inlet and outlet channels, respectively, whereas  $A_1$  and  $A_2$  are the cross-sectional area of the inlet and outlet channels, respectively. The formula indicates that the mean velocity of any cross section is inversely proportional to the cross-sectional area for incompressible channel flow. A description of the fluid velocity between the isosceles trapezoid-shaped pillars would be helpful for the explanation (Fig. S1, ESI†). As shown in Fig. S4A (ESI†), we observed significant variations between the isosceles trapezoid-shaped pillars in the velocity magnitude distribution at  $Re_c = 72.22$ . As expected, numerical simulation results showed that the velocity steeply reached a peak, and then gradually declined after the minimum cross-sectional area increased between the pillars (Fig. S4B, ESI†). The result verified the meaning of the integral form of continuity Equation (6). More importantly, the variational gaps between these pillars result in well-controlled constrictions for cells to pass or reorient, avoiding the potential of nonspecific adsorption caused by prolonged contact between the cells and the pillars. Thus, the proposed structure of the current microfluidic device can prevent cell clogging and long-term cell deformation, which can achieve cell separation with high efficiency and high viability. The fillet radius of the isosceles trapezoid-shaped pillars is helpful in alleviating the cell damage caused by physical collision (Fig. S1, ESI†).

### Inertial separation of microspheres

The focusing mechanism of the fluorescent microspheres in the inertial separation region (Fig. 1C) of the current device was first studied, which served as a theoretical foundation for the optimization of the cell separation conditions. The  $Re_c$  ranging from 0.44 to 125.93 was applied based on the varying characteristic widths of the contraction channel (30, 60, and 90  $\mu\text{m}$ ) and a flow rate of 1 to 170  $\mu\text{L}/\text{min}$ . The representative averaged composite images and fluorescence intensity corresponding to the red dotted lines are shown in Figs. 2 and S5 (ESI†), respectively, which indicate the microsphere (mimic of rare cells) distributions in the inertial separation region under various  $Re_c$ . When the width of the contraction channel was 90  $\mu\text{m}$ , an obvious microsphere distribution band was not observed in the central region of the channel within the whole test range of  $Re_c$  (0.44 to 75.56). This observation may be due to the fact that no sharp width variation for the fluid between the expanding (180  $\mu\text{m}$ ) and contracting (90  $\mu\text{m}$ ) channels was observed, resulting in small area and velocity of the vortex. However, as  $Re_c$  increased, the high speed rotation of vortex flows generated two side cavities of the expansion channel, leading to the microsphere distribution inclining toward the central region of the channel. Particularly, in the case of  $Re_c = 75.56$  ( $Re_p = 3.28$ ), most microspheres passed through the channel central of the inertial separation region. This phenomenon was similar to those in low-aspect ratio (i.e.,

height/width,  $\sim 0.5$ ) rectangular microchannels, where the shear force along the microchannel perimeter is not uniform, leading to preferential microsphere focusing. Thus, strong lift forces acting on microspheres push them to preferentially migrate along the microchannel height before further equilibrating along the microchannel width. Bhagat et al<sup>42</sup> explained that this experimental phenomenology occurred because the shear rate along the rectangular channel height is higher than that along the channel width.

For aspect ratio  $\sim 1$  (width of the contraction channel = 60  $\mu\text{m}$ ), the microspheres were randomly dispersed throughout the inertial separation region (Fig. 2) due to absence of microsphere equilibration at  $Re_c = 0.56$  ( $Re_p = 0.03$ ). In addition, the increasing flow to  $Re_c = 11.11$  ( $Re_p = 0.69$ ) caused two-band microspheres that were laterally and symmetrically focused at the inertial separation region. We believe that most microspheres only moved through the two sides of the cavities of the expansion channels downstream because either no or only a small vortex zone arose at low  $Re_c$ . The other important reason for this phenomenon is that the strong wall effect-induced lift force in the contraction channel acted on the microspheres because their diameters were as large as one-quarter of the contraction channel width compared with that of the expansion channel. While the microspheres pass through series of the contraction and expansion channels, they gradually migrate to both sides of their passage. This phenomenon is the major factor in realizing the separation of different-sized microspheres in a microchannel. Given the lack of geometrical effects of the suddenly contracting and expanding channels, this obvious microsphere distribution was rarely achieved in a straight microchannel under the same conditions. As expected, the microsphere distribution in the inertial separation region changed to pass through the central region of the channel with increasing  $Re_c$  ( $Re_c = 27.78$  to 50), similar to those in a low-aspect ratio multi-orifice microchannel. Interestingly, the microspheres preferred to form a single band concentrated on the centerline of the central channel when  $Re_c = 72.22$  ( $Re_p = 4.51$ ) (Movie S1, ESI†). At high  $Re_c = 94.44$  ( $Re_p = 5.90$ ), a three-band distribution of microspheres was observed in the inertial separation region; the microspheres were dispersed near the centerline and the side walls. The same phenomenon was observed in a straight noncircular channel.<sup>39,43</sup> Notably, when the microspheres formed a nearly linear pattern without severe sudden turns because of the presence of the vortex region as they passed through a straight channel at high  $Re_c$ , the microspheres were influenced away from the walls due to the wall-induced lift force caused by another vortex generated near the walls. Thus, the three-band distribution phenomenon that occurred in the multi-orifice square channels can be similarly explained by the particle equilibrium alteration in a straight square channel. We concluded that these phenomena occurred because the vortex in the cavities region fully developed and the velocity magnitude contouring at the vortex attained a critical value relative to the size of the microspheres and the setting of the microchannels. Thus, when passing through a series of alternating contracting (aspect ratio  $\sim 1$ ) and expanding (aspect ratio  $< 1$ ) geometry channels, different-sized microspheres can be separated by forming into diverse band distribution patterns in the inertial separation region with an optimal critical value.

For aspect ratio  $\sim 2$  (width of the contraction channel =  $30\ \mu\text{m}$ ), the microsphere distributions were nearly consistent with those observed with aspect ratio  $\sim 1$  when the flow rate was  $1\ \mu\text{L}/\text{min}$  or  $20\ \mu\text{L}/\text{min}$  due to the small difference of  $Re_c$  between the two different contraction channels (Table S2, ESI†). More specifically, the microspheres remained evenly distributed

in the inertial separation region (Fig. 2), indicating little migration at  $Re_c = 0.74$  ( $Re_p = 0.10$ ). After increasing the flow rate to  $Re_c = 14.81$  ( $Re_p = 2.08$ ), the lift force permitted the microspheres to overcome the viscous drag. Aside from the influence of the vortex in the expansion channels, the lift force along the contraction channel width is four times greater than that

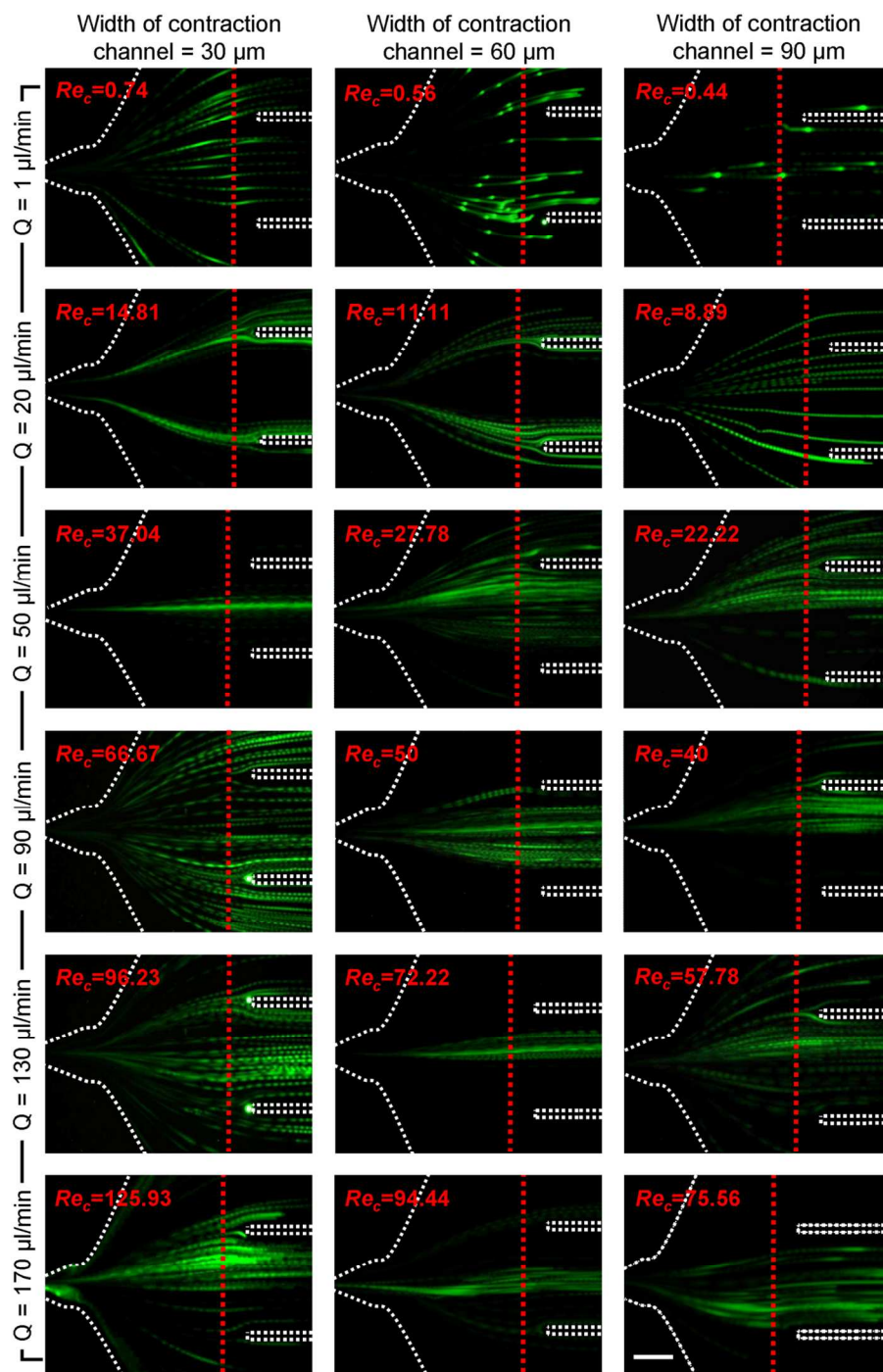


**Fig. 2** One set of fluorescence photographs of fluorescence microsphere trajectories under various  $Re_c$  in the inertial separation region after passing through three different widths of contraction channels ( $30$ ,  $60$ , and  $90\ \mu\text{m}$ ) in the inertial focusing region. The white dotted lines indicate the position of channel walls and elliptical column. The red dotted lines were used to analyze fluorescence microsphere distributions at the same longitudinal positions. The analytical results are listed in Fig. S5 (ESI†). Scale bar,  $200\ \mu\text{m}$ .

along the channel height as a consequence of varying shear rates,<sup>42</sup> which results in high lateral migration of microspheres along the channel width. Thus, at this flow rate ( $Re_c = 14.81$ ;  $Re_p = 2.08$ ), the microspheres began to migrate across the channel cross-section toward two equilibrium positions and focused near the sidewalls. Similar microsphere behavior was also observed at the high-aspect ratio (aspect ratio  $\gg 1$ ) straight rectangular channel.<sup>33,42</sup> However, the straight rectangular channel required higher  $Re_c$  compared with the multi-orifice channel due to the lack of geometrical effects of the suddenly contracting and expanding channels. For  $Re_c = 37.04$  ( $Re_p = 5.21$ ), another obvious change was observed in the microsphere distribution due to the action of the vortex in the cavity region; a central microsphere band was concentrated on the centerline of the center channel region. For  $Re_c > 66.67$  ( $Re_p > 9.38$ ), the microspheres were dispersed near the two sides of the channels and the central channel. In particular, two small vortex zones were formed near the initial part of the inertial separation region when  $Re_c = 125.93$  ( $Re_p = 17.71$ ). The trains of the microspheres were unstable and the spacing between the microspheres in the central and side channels was no longer uniform. The exact origin of this behavior remains unclear and warrants further investigation. However, we believe that the microsphere distributions were likely influenced by the high volume fraction of the microspheres in a high-aspect ratio multi-orifice channel. The movement of microspheres in the contraction channel was clearly affected as a result of the multibody interactions at high  $Re_c$ ; thus, a single-microsphere equilibrium position cannot be formed in the suddenly contracting and expanding narrow channels. The interactions between the microspheres were not negligible, and the transient aggregation of the closely spaced particles likely formed in the narrow contraction channel at high  $Re_c$ ; the same phenomenon was observed by Chun and Ladd in a square duct at high  $Re_c$ .<sup>43</sup> These results indicated that low  $Re_c$  cannot induce microspheres to pass through the central channel of the inertial separation region and high  $Re_c$  can lead to excessive turbulence around the microspheres, so stable equilibrium positions cannot be produced. A single-microsphere band concentrated on the central channel can be formed at a moderate  $Re_c$ , suitable channel aspect ratio, and appropriate microsphere volume fraction.

To precisely analyze microsphere distribution characteristics, the fluorescence intensities of the distributed microspheres, which indirectly represent microsphere distribution (Fig. S5, ESI†), were analyzed. The fluorescence intensity along the red dotted lines (Fig. 2) was analyzed using Image-Pro Plus 6.0 software, from which only three kinds of  $Re_c$  (37.04, 50, and 72.22) were found to promote the formation of the microspheres into a single band in the central channel region (250  $\mu\text{m}$  to 750  $\mu\text{m}$ ). However, in the imaging analysis, the fluorescence intensities of the well-focused fluorescence microspheres captured by the CCD camera were considerably brighter than the fluorescence intensities of the off-focused microspheres, resulting in poor accuracy of the fluorescence intensity magnitude.<sup>31</sup> Therefore, microsphere recovery, defined as the percentage of microspheres successfully sorted from the total number of microsphere within the initial injected fraction, was calculated with the specific ranges of  $Re_c$ . As shown in Table S2 (ESI†), the highest recovery (98.93%) for 30  $\mu\text{m}$  contraction channels can be achieved at  $Re_c = 37.04$  ( $Re_p =$

5.21), the highest recovery (99.42%) for 60  $\mu\text{m}$  contraction channels can be achieved at  $Re_c = 72.22$  ( $Re_p = 4.51$ ), and the highest recovery (88.32%) for 90  $\mu\text{m}$  contraction channels can be achieved at  $Re_c = 75.56$  ( $Re_p = 3.28$ ). However, the optimum  $Re_p$  range for equally sized microspheres changed as contraction channel dimensions changed (Table S2, ESI†). Overall, the optimum results for 30 and 60  $\mu\text{m}$  contraction channels are superior to the existing inertial systems. Considering that the 30  $\mu\text{m}$  contraction channels easily lead to intermittent clogging problems and cannot achieve stable performance, a contraction channel dimension of 60  $\mu\text{m}$  and a value of  $Re_c$  ranging from 50 to 72.22 were chosen for the succeeding sample separation.

### Inertial separation of cells

Cell experiments were first performed to investigate the effects of hematocrit (Hct) on the focusing of blood cells in the multi-orifice microchannel. Human blood is composed of the following three main types of cells: erythrocytes, leukocytes, and platelets. Erythrocytes or RBCs are highly deformable, discoid biconcave-shaped cells with diameters ranging from 6  $\mu\text{m}$  to 8.5  $\mu\text{m}$  and thicknesses ranging from 1.8  $\mu\text{m}$  to 2.8  $\mu\text{m}$ . Leukocytes or WBCs are deformable, nearly spherical cells with diameters larger than 6  $\mu\text{m}$  to 10  $\mu\text{m}$  (granulocytes: 10–15  $\mu\text{m}$ ; lymphocyte: 6–15  $\mu\text{m}$ ; monocyte: 12–20  $\mu\text{m}$ ). Platelets have diameters ranging from 1  $\mu\text{m}$  to 3  $\mu\text{m}$ . To achieve high-separation purity of rare cells, unsuccessful collection of blood cells must be prevented from entering center outlet 1. Generally, whole blood (~40% Hct) is too viscous to achieve Newtonian fluid separation.<sup>44</sup> In addition, high cell density of whole blood will result in increased cell–cell interaction and focusing imbalance. Thus, a dilution procedure for whole blood is necessary. However, working with high Hct is imperative to save time on processing and analysis. To determine the optimum Hct (minimum dilution) that can be processed in a microchannel without affecting the blood cell focusing, tests with diluted whole blood cells (0.5% to 8% Hct) were conducted at the optimum test conditions, which were determined through the above inertial separation of fluorescence microsphere experiments. To obtain clear photographic images of blood cells during the separation process, background images were captured at a certain time interval from the same site in the channel to allow background correction, wherein all pixels with the same value were removed. As a result, high-contrast composite images describing the blood cell equilibration variation were acquired (Fig. S6, ESI†). Figs. S6A and D in ESI† respectively show the blood cell equilibration position and corresponding light intensity assay under different Hct conditions. A central cell-free layer was developed for  $Re_c = 72.22$  at Hct = 0.5%. However, as Hct increased to 2%, a clear central cell band was formed in the multi-orifice microchannel and the corresponding light intensity became stronger because of abundant cell–cell interactions and overlapping at the same  $Re_c$  (Fig. S6, ESI†). When Hct was increased to 8%, the width of the central cell band became wider than when Hct was 2%. Considering that RBCs comprise majority of the blood constituents, the intensity distribution primarily represents the RBC equilibration.<sup>44</sup> This phenomenon can be explained as follows: as the blood cell concentration increases, more blood cells attempt to occupy the same equilibrium positions spontaneously, leading to enhanced cell–cell interactions and greater focusing imbalance. In addition, the

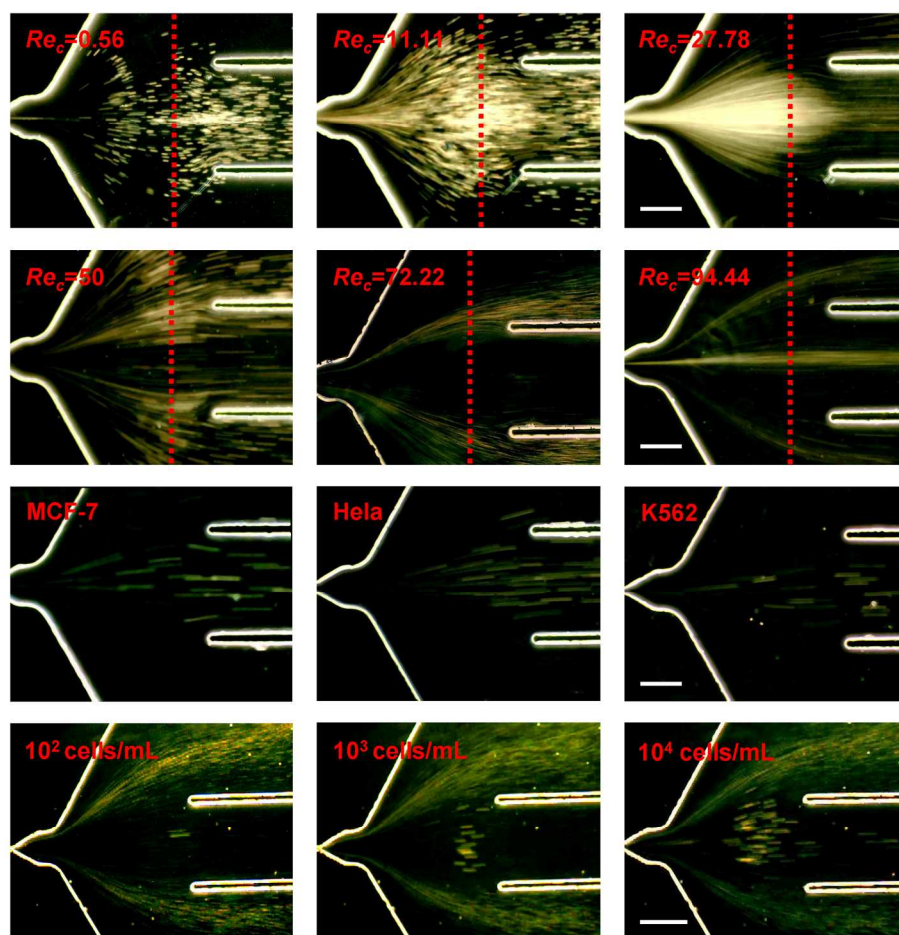


**Fig. 3** Cell trajectories in the inertial separation region under various  $Re_c$ . The first and second rows show blood cell trajectories under various  $Re_c$  values when Hct = 1%. The red dotted lines were used to analyze blood cell distributions at the same longitudinal positions. The analytical results are listed in Fig. S7 (ESI†). The third row shows different rare cell (MCF-7, HeLa, and K562 cells;  $10^4$  cells/mL in PBS working buffer) trajectories at  $Re_c = 72.22$ . The fourth row shows different concentration K562 cell (in 1% Hct blood) trajectories at  $Re_c = 72.22$ . In the study, the width of the contraction channel in the inertial focusing region is 60  $\mu\text{m}$ . Scale bar, 200  $\mu\text{m}$ .

effect of high  $Re_c$  on blood cell equilibration variation at Hct = 2% was investigated, and the light intensity distribution across the channel width was measured using the collected images (Figs. S6B and E, ESI†). The above results illustrate that blood cell equilibration position is not stable at high Hct because of cell focusing imbalance caused by cell–cell interactions and irregular variation of channel resistances. In addition, as  $Re_c$  increases, the width of the central cell-free layer increases (Fig. S6E, ESI†). Based on the above results, 1% Hct was chosen for cell separation in the inertial microfluidic system. The results (Figs. S6C and F, ESI†) show that not all blood cells were focused in the equilibrium positions close to the channel sidewalls in the given channel length (2.4 cm) when  $Re_c = 50$ . However,  $Re_c = 72.22$  can provide good focus for blood cells, forming a clear 60  $\mu\text{m}$  (in width) central cell-free layer at Hct = 1% [the width was obtained by measuring the full width at half maximum (FWHM) of the distance between the two cell-occupied regions]. As  $Re_c$  increases, the large inertial lift forces enable the cells to overcome the drag forces better, and more cells are induced to focus toward the channel sidewalls. Interestingly,

when  $Re_c$  was increased to 94.44, three cell-band distributions with  $\sim 10$   $\mu\text{m}$  width were observed (Movie S2, ESI†). The width of the cell-band was determined by measuring the FWHM of the region occupied by the blood cells. To our knowledge, this is the first illustration of three-band blood cell distribution in a multi-orifice microchannel at high  $Re_c$ . We concluded that this phenomenon occurred because the lateral migration of blood cells is influenced by inertial lift forces and unique secondary flow at high  $Re_c$ , and the equilibrium position lies on the center or corner of side walls similar to equilibrium alteration in a straight square channel.<sup>42</sup> In addition, two side peaks that were 50  $\mu\text{m}$  away from the channel sidewalls were observed to exhibit higher intensity than that of the central peak (Fig. S6F, ESI†), similar to a previous study in a straight microchannel.<sup>42</sup>

Additionally, the optimum  $Re_c$  range was obtained by measuring blood cell trajectories in the inertial separation region at Hct = 1% (Fig. 3). Blood cells were spread out over a wide area and inclined to concentrate on the centerline in the central channel region at a low  $Re_c$  ( $Re_c \leq 27.78$ ) (Fig. 3). Thus, the highest peak representing the maximum light intensity of cells

(Fig. S7, ESI†) was also located at the centerline of the central channel region. The longitudinal distribution width of blood cells in the central channel region became narrower from  $\sim 800 \mu\text{m}$  to  $\sim 600 \mu\text{m}$  as  $Re_c$  increased from 11.11 to 27.78. Meanwhile, a white region corresponding to a mass of red blood cells in the captured images appeared at  $Re_c \leq 27.78$ , which resulted from abundant cell–cell interactions and overlapping. As  $Re_c$  increased, the blood cells from the inertial focusing region became bifurcated ( $Re_c = 50$ ), clearly split into two groups entering their respective side channels ( $Re_c = 72.22$ ), and formed a three-band distribution ( $Re_c = 94.44$ ) (Fig. 3). The formation of the three-band distribution at  $Re_c = 94.44$  is unfavorable for separation because the rare cell enrichment efficiency will be decreased. Based on the above results, a  $Re_c$  of 72.22 was preliminarily chosen as the optimum condition for blood cell focusing in the inertial separation region, which was also the optimum condition for the inertial focusing region.

In the case of the three rare cells MCF-7, K562, and HeLa, the optimum  $Re_c$  was used and was achieved by separation of fluorescence microspheres in the inertial separation. Fig. 3 shows the MCF-7, HeLa, and K562 cell trajectories in the inertial separation region after flowing through the multi-orifice microchannel at  $Re_c = 72.22$ . The cell streamlines were finely focused in the central channel region. After conducting independent flow measurements of the rare cells, each kind of fluorescently labeled rare cell was spiked into unstained  $40 \times$  diluted whole blood and subsequently applied to  $Re_c$  measurements. High-speed movement cells could not be imaged well at extremely short exposure times because of their lower fluorescence intensities compared with the fluorescent microspheres, so only bright-field images permitting enhanced visualization were taken. Fig. 3 illustrates that K562 cells with different concentrations were successfully separated from 1% Hct blood, and almost all of the low-concentration ( $10^2$  cells/mL) K562 cells passed through the central channel region (Movie S3, ESI†). The above phenomenon can be explained as follows: the highly concentrated K562 cells attempt to occupy the same equilibrium positions spontaneously, resulting in focusing dispersion and ideal flow pattern disturbance caused by their surrounding flow field change. Consequently, we believe that when the multi-orifice microchannel is sufficiently longer (2.4 cm) than the narrow width of the channel ( $60 \mu\text{m}$  or  $180 \mu\text{m}$ ), the cell–cell interactions that affect cell focusing behavior and deteriorate separation efficiency cannot be disregarded even with 1% Hct blood cells. Similar results were obtained in a snake-shaped channel in a study by Tanaka.<sup>45</sup> These results suggested that aside from  $Re_c$ , equilibrium positions of cells vary depending on their concentration and channel-to-cell size ratio ( $D_h/d$ ).<sup>45,46</sup> At low sample concentration, an equilibrium position driven from the interaction of drag force and inertial lift force moves toward the wall as  $Re_c$  increases. Afterward, at a constant  $Re_c$ , this equilibrium position shifts toward the centerline as  $D_h/d$  decreases. Estimating the equilibrium position variation for a high-concentration sample in the multi-orifice microchannel is difficult. In addition to sample concentration, sample shape and deformability are also important factors affecting the equilibrium position.

Tumor cells not only have larger volume and cellular karyon

but also have better deformability compared with solid microspheres.<sup>22</sup> Furthermore, multicellular CTC clusters yielding important prognostic significance have been reported in clinical samples.<sup>6,40</sup> Therefore, the equilibrium position of tumor cells are different from rigid microparticles under the same separation conditions. More specifically, deformable cells experience deformation-induced lift force compared with rigid microspheres, and differently shaped cells may respond differently to inertial forces in the applied flow field.<sup>35</sup> In addition, unlike rigid microspheres whose sizes are evenly controlled, cells have relatively wide distribution (Fig. S8, ESI†). All the above issues limit the enrichment efficiency of rare cells in the inertial separation region. Therefore, a central channel dimension with a width of  $500 \mu\text{m}$  was used to collect the target cells efficiently and to avoid the loss of some small and irregular rare cells, especially CTC clusters. However, in the present case, this situation would aggravate the condition of blood cells, especially for some leukocytes, which have overlapping sizes with heterogeneous rare cells. It may also pose a contamination problem for the target cells and decrease the performance of the designed device. Therefore, in the current device, a steric hindrance structure was designed and connected with the central channel of the inertial separation region to achieve high-purity separation of rare cells.

#### Steric hindrance separation of microspheres and cells

Microsphere trajectories in the steric hindrance region were first measured under optimum conditions. In the case without  $\mu\text{ITPAR}$  (Fig. 4A), when  $Re_c = 27.78 - 50$ , microspheres were distributed throughout the expansion region. A three-band microsphere distribution phenomenon was observed, which can be similarly explained by microsphere equilibrium alteration because of the sudden decrease in resistance in the two side-outlet regions (Fig. 1). The two empty spaces between the central band and the two side bands became wider as  $Re_c$  increased. However, when  $Re_c = 72.22$ , the empty spaces disappeared and the microspheres maintained a straight movement. The above results can be explained as follows: with increased  $Re_c = 72.22$ , the high-velocity microspheres attempted spontaneously to concentrate on the centerline equilibrium positions in the inertial separation region, so the subsequent resistance change in the steric hindrance region cannot change the direction of the microsphere motion within a short time. However, the width of the central band became wider than that of the inertial separation region (Fig. S9, ESI†), which is highly unfavorable for sample separation, especially for irregular cells. Therefore, in the current device, a unique combination of MOFF and  $\mu\text{ITPAR}$  was used to achieve maximum target sample recovery. As shown in Fig. 4B, at  $Re_c = 27.78$  to 50 in device 1 (Table S1, ESI†), poorly focused microspheres were stopped by  $\mu\text{ITPAR}$ . The central band microsphere distribution became narrower and more concentrated on the centerline equilibrium positions as  $Re_c$  increased. When  $Re_c = 72.22$ , the microspheres inclined to form a single band and concentrated on the centerline in the steric hindrance region, consistent with the inertial focusing principle (Movie S4, ESI†). However, few poorly focused microspheres were unable to immobilize in the gaps between microposts and were also guided along the micropost array rails into the final outlet at  $Re_c = 72.22$  (short arrows in Fig. 4C). The above phenomenon can be

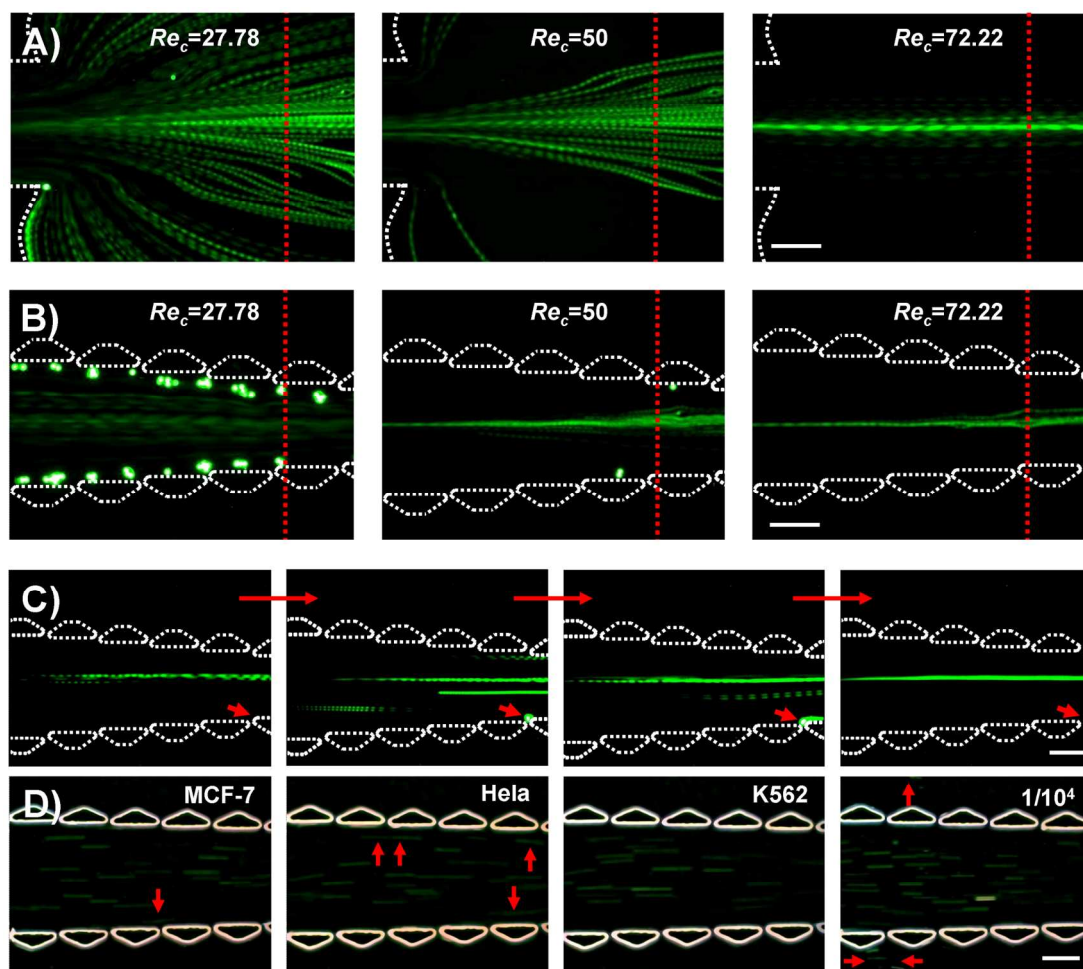


**Fig. 4** Microsphere (A, B and C) and various cell (D) trajectories in the steric hindrance region. (A) and (B): microsphere trajectories under different  $Re_c$  in the steric hindrance region without (A) and with (B) the structure of  $\mu$ ITPAR. The red dotted lines were used to analyze fluorescence microsphere distributions at the same longitudinal positions. The analytical results are listed in Fig. S9 (ESI<sup>†</sup>). (C) Sequential micrographs of microspheres are railed without being immobilized in the steric hindrance region at  $Re_c = 72.22$ . The long red arrows represent the sequential direction of the micrographs. The short red arrows show that the poorly focused microspheres were well railed without moving away from the steric hindrance region (for the detailed process, see Movie S4, ESI<sup>†</sup>). (D) From left to right: trajectories of rare cells (MCF-7, HeLa, and K562 cells;  $10^4$  cells/mL in PBS working buffer) and MCF-7 cells (spiked in 1% Hct blood; cells-to-blood cell ratio is  $1/10^4$ ) in the steric hindrance region at  $Re_c = 72.22$ . The red arrows indicate that the filtered cells were railed by the micropost array. Scale bar, 200  $\mu$ m.

explained as follows: the radius of fluorescent microspheres (7.5  $\mu$ m) is larger than the line offset (5  $\mu$ m), which promotes the movement of microspheres along the micropost array rails. Furthermore, the velocity vector of microspheres is parallel to the direction of the centerline at the optimum  $Re_c$  (72.22), so microspheres entering the gaps between each two micropost pillars with a clogging angle are avoided. The obtained results are similar with previously reported findings.<sup>47</sup>

Based on the observation of microsphere separation, the moving trajectories of MCF-7, HeLa, and K562 cells in the steric hindrance region after flowing through the inertial separation region were investigated (Fig. 4D). As discussed above, irregularly shaped rare cells, especially high-concentration rare cells, cannot form a single central band concentrated on the centerline of the steric hindrance region (Movie S5, ESI<sup>†</sup>). However, the microposts in the device can guide the poorly

focused cells to move along  $\mu$ ITPAR, which improves cell recovery. In the case of mixed samples (i.e., rare cells in diluted whole blood), when the rare cells and unseparated blood cells from the inertial separation region entered the central channel of the steric hindrance separation, the unseparated blood cells were filtered by the microfluidic array rails. In the current device, the minimum space (10  $\mu$ m) between two pillars was designed to be smaller than the diameter of rare cells, but larger than the small or highly deformable blood cells. Therefore, after the steric hindrance separation the rare cells were transported through rails into center outlet 1, other small or highly deformable blood cells were transited into the two side-outlets (Fig. 4D). In addition, compared with traditional filtration techniques, the  $\mu$ ITPAR used in the current device can effectively avoid the problem of clogging or jamming. Given that the fluidic flow direction in the traditional dead-end filtration is

perpendicular to the filtration structures, some larger and stiffer samples cannot pass through the barriers, leading to clogging. By contrast, in the current device, the fluidic flow direction is nearly parallel to the filtration rails, which prevents the problem of jamming. In addition, traditional dead-end filtrations limited the ability to achieve high-throughput separation. However, in the current device, a large number of blood cells were removed by inertial separation before entering the rail array region, eventually achieving high-throughput and high-efficiency separation.

#### 10 Isolation efficiency and cell viability

To comprehensively evaluate the device performance, the isolation efficiency of each independent sample (microsphere, K562 cells, and blood cells) was calculated in different settings of  $\mu$ ITPAR (i.e., Devices 1, 2, and 3, Table S1 in ESI†) with specific ranges of  $Re_c$  (Fig. S10, ESI†). First, the collection efficiencies of microspheres were found to be greater than the collection efficiency of K562 cells at the same separation conditions regardless of the  $\mu$ ITPAR patterned. As expected, these observations were ascribed to the existence of cellular heterogeneity in cell sizes and types (Fig. S8, ESI†), which affected the quality of the separation. Additionally, compared with devices 2 and 3, device 1 can achieve preferable collection efficiency for microspheres/K562 cells. The reason is that the short line offset promotes the movement of microspheres/K562 cells along the micropost array rails. Device 1 can effectively reduce blood cell recovery in center outlet 1 without affecting the target cell collection efficiency relative to the control groups, which agrees well with our observations on sample trajectories in the steric hindrance region. Finally, the optimum  $Re_c$  for blood cell separation is verified to be 72.22, which is similar to our previous observations on blood cell trajectories. Unfortunately, the maximum collection efficiency for the high-concentration ( $10^4$  cells/mL) K562 cells were achieved at  $Re_c = 83.33$  (Fig. S10, ESI†). Therefore, the collection efficiency of K562 cells with different concentrations spiked in diluted whole blood were measured under the two flow conditions, i.e.,  $Re_c = 72.22$  and 83.33 (Fig. 5A). Unexpectedly, similar collection efficiencies for low-concentration K562 cells ( $<10^3$  cells/mL) can be obtained under the two different  $Re_c$  conditions, possibly because of decreased interactions between rare cells in a low cell concentration, generating preferable inertial focusing under a short and specific range of  $Re_c$ . Thus, tests for each independent cell sample (in this study,  $1/10^6$  ratio of rare cells-to-blood cells was used to mimic the low-abundance rare cells in diluted whole blood) were conducted under optimum  $Re_c$  (i.e.,  $Re_c = 72.22$ ) and high rare cell collection efficiency ( $>90\%$ ) and enrichment efficiency ( $>2.02 \times 10^5$ -fold) for the three rare cells MCF-7, HeLa, and K562 (Fig. 5B). As expected, this enrichment efficiency is much higher than that ( $>1.64 \times 10^3$ -fold) of the microfluidic system without steric hindrance region (Fig. S11). A set of representative images for leukemic cells input in the inlet and collected in the different outlets is shown in Fig. S12 (ESI†). In addition, the ability of the current device to isolate large MCF-7 cells (average diameter of approximately  $18.8 \pm 2.3 \mu\text{m}$ ) was found to be more favorable ( $94.9 \pm 2.69\%$  collection efficiency) than the relatively small K562 cells (average diameter around  $16.8 \pm 2.1 \mu\text{m}$ ) and HeLa cells (average diameter of approximately  $14.6 \pm 2.8 \mu\text{m}$ ). The collection efficiencies of

K562 and HeLa cells were almost similar, i.e.,  $91.8 \pm 2.08\%$  for K562 cells and  $90.2 \pm 4.39\%$  for HeLa cells. The reasons for the different collection efficiencies of the three rare cells may be their deformability, which possibly exerted some secondary effects on cell separation, except for cell size, which required further verification using the current integrated system. Although the current system has the ability to isolate a highly heterogeneous mix of rare cells, a small amount of rare cells (e.g., HeLa cells) with diameters smaller than  $10 \mu\text{m}$  are inevitably lost in the waste outlets (outlets 2 and 3).

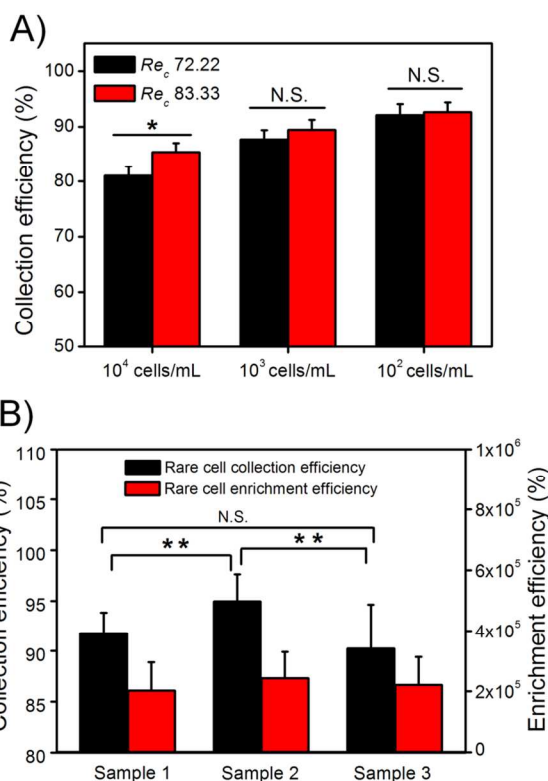


**Fig. 5** Evaluation of microfluidic system performance using rare cells (K562, MCF-7, and HeLa cells). (A) Comparison of the collection efficiency for different concentration K562 cells in diluted whole blood (1% Hct) at varied flow conditions. (B) Statistical results of collection efficiency and enrichment efficiency of rare cells at rare cell-to-blood cell ratio of  $1/10^6$ . Each type of independent rare cell spiked into diluted whole blood (sample 1, K562 cells; sample 2, MCF-7 cells; and sample 3, HeLa cells) was tested using optimum test conditions (1% Hct blood and  $Re_c = 72.22$ ). Standard deviations deduced from ten parallel experiments are shown as the error bars, with the significance assessed by ANOVA.  $**P < 0.01$ ;  $*P < 0.05$ ; N.S., not significant.

Considering that some poorly focused rare cells underwent small deformations because of high shear stress, the viability and integrity of the collected cells must be considered. After separation, rare cell viability was determined by reseeding cells back into culture to observe their morphologies and extent of proliferation. The results (Fig. S13, ESI†) show that the morphology and proliferation rate of the collected rare cells were analogous to the control cells, and no noticeable changes were observed. In addition, culture of sorted rare cells stained using

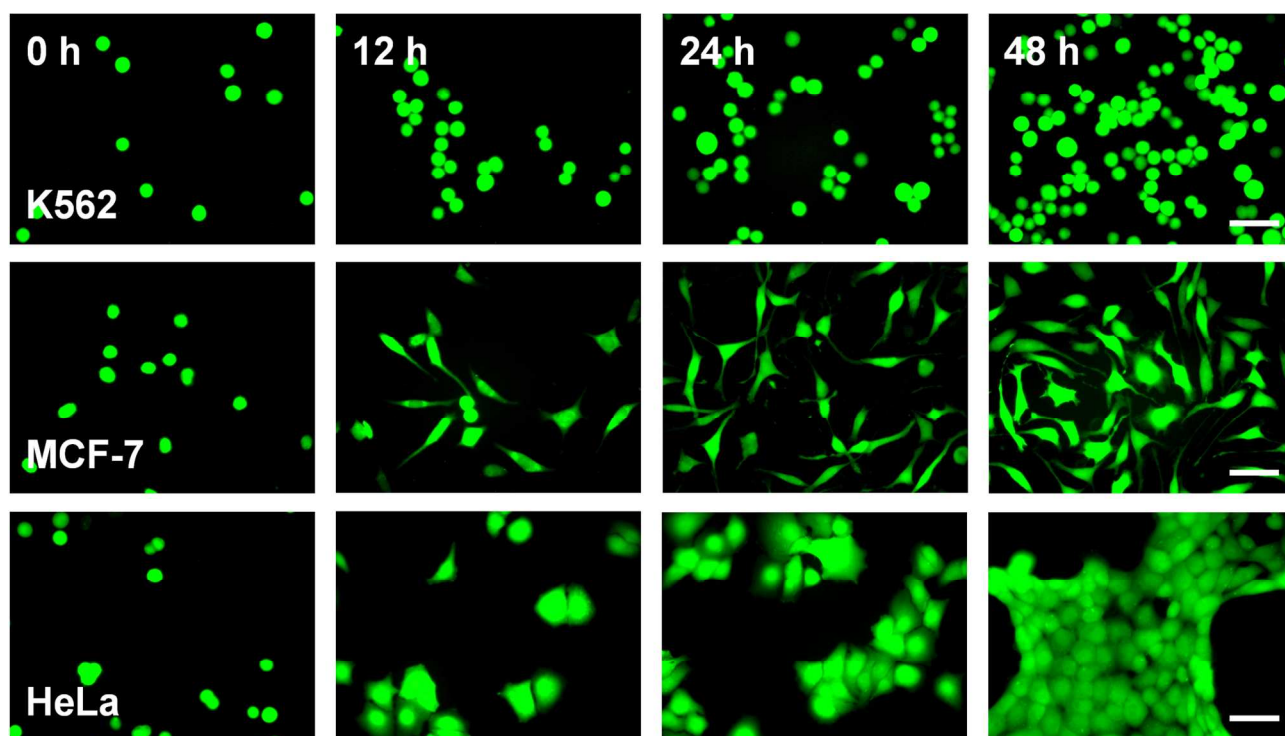


**Fig. 6** Cellular viability assay of isolated rare cells (K562, MCF-7, and HeLa cells) by reseeding them back in culture for 48 h. In this study, the rare cells ( $10^4$  cells/mL, spiked in 1% Hct blood) were all stained with CellTracker Green before separation to easily distinguish them from the blood cells. Scale bar, 50  $\mu$ m.

CellTracker Green in a 96-well plate (Fig. 6) was successfully performed. Particular attention was given to the separated HeLa cells, demonstrating that the device can successfully separate aggregated cancer cells similar to CTC clusters despite high flow conditions (Fig. 6). This phenomenon may be caused by the short transit time within the channel, which prevents breakup of the cell clusters. Cell viability was further assessed using a common AO/PI double-staining protocol.<sup>30,48</sup> As a result, > 92% viable cells were retrieved for all three rare cells, indicating that high shear stress does not compromise cell viability (Fig. S14, ESI†). The obtained results confirm that the developed multistage technology exerts minimal effects on cell viability during high-speed separation process. The obtained results also illustrate that the microfluidic device developed in this study has the potential to obtain high-purity and high-viability rare cells. In addition, unlike other types of microfluidic rare cell separation systems, which only allow on-chip growth of cells, inherently limiting their ability to couple with conventional biological assays or other downstream applications platforms, the present passive cell separation technique can achieve continuous sorting, allowing easy retrieval of rare cells that remain intact and viable. Therefore, this technique could be used for downstream rare cell analysis, such as cell culture, gene analysis, drug screening and cancer prognosis.

## Conclusions

In this study, a passive multistage microfluidic device was developed using a unique combination of inertial microfluidics

and steric hindrance. The serial complementary combination of the two different mechanism sorting methods achieved high-throughput and highly sensitive cell separation. The separation and focusing mechanism of this microfluidic system were discussed using comprehensive numerical model of velocity field fluctuations and experimental studies of fluorescence-labeled microspheres. As an actual application of this microfluidic system, tumor cells (MCF-7 and HeLa cells) and leukemic (K562) cells spiked into 1% Hct blood were successfully separated with throughput of  $2.24 \times 10^7$  cells/min, cell recovery of > 90%, and an impressive cell enrichment of  $> 2.02 \times 10^5$ -fold. Compared with existing rare cell isolation technologies, the current microfluidic device possesses high throughput, cell recovery, and cell enrichment. In addition, the microfluidic platform was only driven by purely hydrodynamic forces, which prevents the integration of complex external force fields, making the device easy to fabricate and operate. Although sample dilutions similar to existing separation technologies are required to reduce blood viscosity and avoid channel blocking, the simple channel design in the current device allows for easy multiplex cascading of separation circuits in parallel, in series, and in lamination layers, with the ability to analyze milliliters of clinical blood samples within a short period of time. Along with the trend of combining multiple rare cell separation methods on a single device, the innovative strategy of combining inertial microfluidics and steric hindrance could be used to sort a variety of rare cells with higher efficiency, indicating significant potential for numerous areas of sample preparation in fundamental studies and clinical diagnoses.

## Acknowledgements

This study was supported by the National Natural Science Foundation of China (21175107 and 21375106), the Ministry of Education of the People's Republic of China (NCET-08-602 0464), the Fundamental Research Funds for the Central Universities (Z109021303), the Scientific Research Foundation for the Returned Overseas Chinese Scholars, the State Education Ministry, and the Northwest A&F University.

## Notes and references

- <sup>10</sup> <sup>a</sup> College of Science, Northwest A&F University, Yangling, Shaanxi, 712100, China. Fax: +86-298-708-2520; Tel: +86-298-708-2520; E-mail: jywang@mwsuaf.edu.cn
- <sup>b</sup> College of Veterinary Medicine, Northwest A&F University, Yangling, Shaanxi, 712100, China
- <sup>15</sup> † Electronic Supplementary Information (ESI) available: Materials and methods, supplementary Figs. S1–S13 and Tables S1–S2. See DOI: 10.1039/b000000x/
- 1 M. Toner and D. Irimia, *Annu. Rev. Biomed. Eng.*, 2005, **7**, 77–103.
- 2 U. Dharmasiri, M. A. Witek, A. A. Adams and S. A. Soper, *Annu. Rev. Anal. Chem.*, 2010, **3**, 409–431.
- 3 M. Cristofanilli, G. T. Budd, M. J. Ellis, A. Stopeck, J. Matera, M. C. Miller, J. M. Reuben, G. V. Doyle, W. J. Allard, L. M. Terstappen and D. F. Hayes, *N. Engl. J. Med.*, 2004, **351**, 781–791.
- 4 C. Wittekind and M. Neid, *Oncology*, 2005, **69**, 14–16.
- <sup>25</sup> 5 W. J. Allard, J. Matera, M. C. Miller, M. Repollet, M. C. Connelly, C. Rao, A. G. J. Tibbe, J. W. Uhr and L. W. M. Terstappen, *Clin. Cancer Res.*, 2004, **10**, 6897–6904.
- 6 H. W. Hou, M. E. Warkiani, B. L. Khoo, Z. R. Li, R. A. Soo, D. S.-W. Tan, W.-T. Lim, J. Han, A. A. S. Bhagat and C. T. Lim, *Sci. Rep.*, 2013, **3**, 1259.
- <sup>30</sup> 7 A. A. S. Bhagat, H. Bow, H. W. Hou, S. J. Tan, J. Han and C. T. Lim, *Med. Biol. Eng. Comput.*, 2010, **48**, 999–1014.
- 8 R. Kalluri and R. A. Weinberg, *J. Clin. Invest.*, 2009, **119**, 1420–1428.
- <sup>35</sup> 9 C. V. Pecot, F. Z. Bischoff, J. A. Mayer, K. L. Wong, T. Pham, J. Bottsford-Miller, R. L. Stone, Y. G. Lin, P. Jaladurgam, J. W. Roh, B. W. Goodman, W. M. Merritt, T. J. Pircher, S. D. Mikolajczyk, A. M. Nick, J. Celestino, C. Eng, L. M. Ellis, M. T. Deavers and A. K. Sood, *Can. Dis.*, 2011, **1**, 580–586.
- <sup>40</sup> 10 L. Zhang, L. D. Ridgway, M. D. Wetzel, J. Ngo, W. Yin, D. Kumar, J. C. Goodman, M. D. Groves and D. Marchetti, *Sci. Transl. Med.*, 2013, **5**, 180ra48.
- 11 X. Mu, W. Zheng, J. Sun, W. Zhang and X. Jiang, *Small*, 2013, **9**, 9–21.
- <sup>45</sup> 12 A. A. S. Bhagat, H. W. Hou, L. D. Li, C. T. Lim and J. Han, *Lab Chip*, 2011, **11**, 1870–1878.
- 13 W. Chen, S. Weng, F. Zhang, S. Allen, X. Li, L. Bao, R. H. W. Lam, J. A. Macoska, S. D. Merajver and J. Fu, *Acs Nano*, 2012, **7**, 566–575.
- <sup>50</sup> 14 M. S. Kim, T. S. Sim, Y. J. Kim, S. S. Kim, H. Jeong, J.-M. Park, H.-S. Moon, S. I. Kim, O. Gurel, S. S. Lee, J.-G. Lee and J. C. Park, *Lab Chip*, 2012, **12**, 2874–2880.
- 15 H. Mohamed, M. Murray, J. N. Turner and M. Caggana, *J. Chromatogr. A*, 2009, **1216**, 8289–8295.
- <sup>55</sup> 16 A. E. Saliba, L. Saias, E. Psychari, N. Minc, D. Simon, F. C. Bidard, C. Mathiot, J.-Y. Pierga, V. Fraissier, J. Salamero, V. Saada, F. Farace, P. Vielh, L. Malaquin and J.-L. Viovy, *Proc. Natl. Acad. Sci. U. S. A.*, 2010, **107**, 14524–14529.
- 17 S. K. Arya, B. Lim and A. R. A. Rahman, *Lab Chip*, 2013, **13**, 1995–2027.
- <sup>60</sup> 18 D. R. Gossett, H. T. K. Tse, J. S. Dudani, K. Goda, T. A. Woods, S. W. Graves and D. Di Carlo, *Small*, 2012, **8**, 2757–2764.
- 19 G. Guan, L. Wu, A. A. S. Bhagat, Z. Li, P. C. Chen, S. Chao, C. J. Ong and J. Han, *Sci. Rep.*, 2013, **3**, 1475.
- <sup>65</sup> 20 M. E. Warkiani, G. Guan, B. L. Khoo, W. C. Lee, A. A. S. Bhagat, P. K. Chaudhuri, D. S.-W. Tan, W.-T. Lim, S. C. Lee, P. C. Y. Chen, C. T. Lim and J. Han, *Lab Chip*, 2014, **14**, 128–137.
- 21 C. W. Schaeffer, A. W. Partin, W. B. Isaacs, D. S. Coffey and J. T. Isaacs, *Prostate*, 1994, **25**, 249–265.
- <sup>70</sup> 22 D. Marrinucci, K. Bethel, R. H. Bruce, D. N. Curry, B. Hsieh, M. Humphrey, R. T. Krivacic, J. Kroener, L. Kroener, A. Ladanyi, N. H. Lazarus, J. Nieva and P. Kuhn, *Hum. Pathol.*, 2007, **38**, 514–519.
- 23 X. Chen, D. F. Cui, C. C. Liu and H. Li, *Sens. Actuators B*, 2008, **130**, 216–221.
- <sup>75</sup> 24 J. Sun, M. Li, C. Liu, Y. Zhang, D. Liu, W. Liu, G. Hu and X. Jiang, *Lab Chip*, 2012, **12**, 3952–3960.
- 25 H. Wei, B. Chueh, H. Wu, E. W. Hall, C. Li, R. Schirrhagl, J.-M. Lin and R. N. Zare, *Lab Chip*, 2011, **11**, 238–245.
- 26 T. Gerhardt, S. Woo and H. Ma, *Lab Chip*, 2011, **11**, 2731–2737.
- <sup>80</sup> 27 S. M. McFaul, B. K. Lin and H. Ma, *Lab Chip*, 2012, **12**, 2369–2376.
- 28 H.-S. Moon, K. Kwon, S.-I. Kim, H. Han, J. Sohn, S. Lee and H.-I. Jung, *Lab Chip*, 2011, **11**, 1118–1125.
- 29 A. J. Mach and D. Di Carlo, *Biotechnol. Bioeng.*, 2010, **107**, 302–311.
- <sup>85</sup> 30 W. Liu, L. Li, J. C. Wang, Q. Tu, L. Ren, Y. Wang and J. Wang, *Lab Chip*, 2012, **12**, 1702–1709.
- 31 J.-S. Park and H.-I. Jung, *Anal. Chem.*, 2009, **81**, 8280–8288.
- 32 P. G. Saffman, *J. Fluid Mech.*, 1965, **22**, 385–400.
- 33 J. Zhou and I. Papautsky, *Lab Chip*, 2013, **13**, 1121–1132.
- 34 J.-S. Park, S.-H. Song and H.-I. Jung, *Lab Chip*, 2009, **9**, 939–948.
- <sup>90</sup> 35 S. C. Hur, N. K. Henderson-MacLennan, E. R. B. McCabe and D. Di Carlo, *Lab Chip*, 2011, **11**, 912–920.
- 36 D. Jiang, D. Sun, N. Xiang, K. Chen, H. Yi and Z. Ni, *Biomicrofluidics*, 2013, **7**, 034113.
- <sup>95</sup> 37 J. Zhang, M. Li, W. H. Li and G. Alici, *J. Micromech. Microeng.*, 2013, **23**, 085023.
- 38 L. Zeng, F. Najjar, S. Balachandrar and P. Fischer, *Phys. Fluids*, 2009, **21**, 033302.
- 39 D. Di Carlo, D. Irimia, R. G. Tompkins and M. Toner, *Proc. Natl. Acad. Sci. U. S. A.*, 2007, **104**, 18892–18897.
- <sup>100</sup> 40 S. L. Stott, C.-H. Hsu, D. I. Tsukrov, M. Yu, D. T. Miyamoto, B. A. Waltman, S. M. Rothenberg, A. M. Shah, M. E. Smas, G. K. Korir, F. P. Floyd, A. J. Gilman, J. B. Lord, D. Winokur, S. Springer, D. Irimia, S. Nagrath, L. V. Sequist, R. J. Lee, K. J. Isselbacher, S. Maheswaran, D. A. Haber and M. Toner, *Proc. Natl. Acad. Sci. U. S. A.*, 2010, **107**, 18392–18397.
- <sup>105</sup> 41 A. J. Mach, J. H. Kim, A. Arshi, S. C. Hur and D. Di Carlo, *Lab Chip*, 2011, **11**, 2827–2834.
- 42 A. A. S. Bhagat, S. S. Kuntaegowdanahalli and I. Papautsky, *Microfluid. Nanofluid.*, 2009, **7**, 217–226.
- <sup>110</sup> 43 B. Chun and A. J. C. Ladd, *Phys. Fluids*, 2006, **18**, 031704.
- 44 J. Zhou, P. V. Giridhar, S. Kasper and I. Papautsky, *Lab Chip*, 2013, **13**, 1919–1929.
- 45 T. Tanaka, T. Ishikawa, K. Numayama-Tsuruta, Y. Imai, H. Ueno, N. Matsuki and T. Yamaguchi, *Lab Chip*, 2012, **12**, 4336–4343.
- <sup>115</sup> 46 K. Gotoh, *Nature*, 1970, **225**, 848–850.
- 47 R. D. Sochol, S. Li, L. P. Lee and L. Lin, *Lab Chip*, 2012, **12**, 4168–4177.
- 48 L. Wang, W. Liu, Y. Wang, J. C. Wang, Q. Tu, R. Liu and J. Wang, *Lab Chip*, 2013, **13**, 695–705.